Thermocapillary migration of a planar droplet at moderate and large Marangoni numbers

Zuo-Bing Wu & Wen-Rui Hu

Acta Mechanica

ISSN 0001-5970
Volume 223
Number 3

Acta Mech (2012) 223:609-626
DOI 10.1007/s00707-011-0587-7

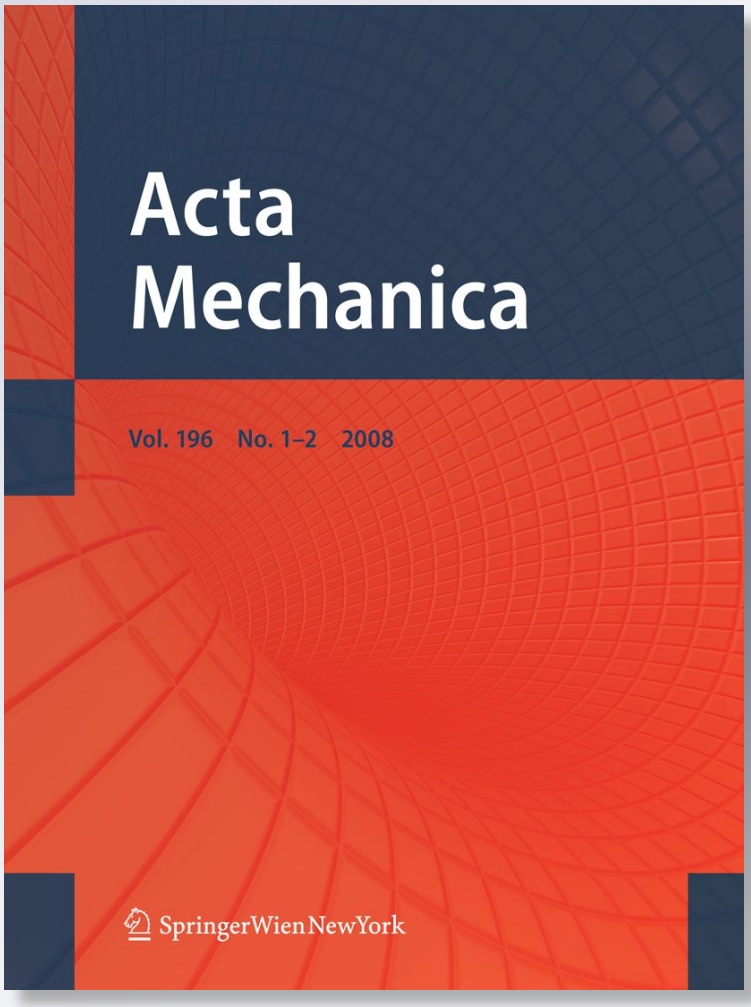

Springer

Acta Mech 223, 609–626 (2012)
DOI 10.1007/s00707-011-0587-7

Zuo-Bing Wu · Wen-Rui Hu

Thermocapillary migration of a planar droplet at moderate and large Marangoni numbers

Received: 27 June 2011 / Revised: 14 November 2011 / Published online: 8 December 2011

Abstract Thermocapillary migration of a planar non-deformable droplet in flow fields with two uniform temperature gradients at moderate and large Marangoni numbers is studied numerically by using the front-tracking method. It is observed that the thermocapillary motion of planar droplets in the uniform temperature gradients is steady at moderate Marangoni numbers, but unsteady at large Marangoni numbers. The instantaneous migration velocity at a fixed migration distance decreases with increasing Marangoni numbers. The simulation results of the thermocapillary droplet migration at large Marangoni numbers are found in qualitative agreement with those of experimental investigations. Moreover, the results concerned with steady and unsteady migration processes are further confirmed by comparing the variations of temperature fields inside and outside the droplet. It is evident that at large Marangoni numbers the weak transport of thermal energy from outside of the droplet into inside cannot satisfy the condition of a steady migration process, which implies that the advection around the droplet is a more significant mechanism for heat transfer across/around the droplet at large *Ma* numbers. Furthermore, from the condition of overall steady-state energy balance in the flow domain, the thermal flux across its surface is studied for a steady thermocapillary droplet migration in a flow field with uniform temperature gradient. By using the asymptotic expansion method, a non-conservative integral thermal flux across the surface is identified in the steady thermocapillary droplet migration at large Marangoni numbers. This non-conservative flux may well result from the invalid assumption of a quasi-steady state, which indicates that the thermocapillary droplet migration at large Marangoni numbers cannot reach a steady state and is thus an unsteady process.

1 Introduction

The transport phenomenon of droplets/bubbles in a liquid is a very important topic for both fundamental hydrodynamics and practical applications such as production of pure materials in manufacturing industry and mass transfer in chemical engineering. Under normal gravity, the motion of droplet/bubbles results from the buoyancy when the densities of two fluids are different. With fast development of space exploration, the studies on the physical mechanism of droplet/bubble migration phenomena under reduced gravity become more and more important. In this case, the buoyant effect vanishes, the droplet/bubble moves as a result of the variance

Z.-B. Wu (✉)
State Key Laboratory of Nonlinear Mechanics, Institute of Mechanics, Chinese Academy of Sciences,
Beijing 100190, China
E-mail: wuzb@lnm.imech.ac.cn
Tel.: +86-10-82543955
Fax: +86-10-82543977

W.-R. Hu
National Microgravity Laboratory, Institute of Mechanics, Chinese Academy of Sciences,
Beijing 100190, China

of the interface tension. Thus, in the microgravity environment, a droplet/bubble suspended in an ambient fluid will move in the direction of the temperature gradient due to thermocapillary force [1]. Thermocapillary motion of a single droplet was firstly examined both theoretically and experimentally by Young et al. [2]. They gave an analytical prediction on its migration speed in the limit case of zero Reynolds (*Re*) and zero Marangoni (*Ma*) numbers, which is called the YGB model. Since then, the thermocapillary migration of a bubble has been studied extensively by a series of theoretical analyses [3–6], numerical simulations [7–10] and experimental investigations [11]. In the mean time, several numerical techniques for treating the two-phase flow, such as the front-tracking method [12,13] and the level-set method [14], have also been developed, which may provide effective techniques to directly investigate thermocapillary migration processes of bubbles or droplets [15–18], interfacial mass transfer [19,20] and interfacial flows with soluble surfactants [21,22].

For the migration of a droplet, the experimental result for the migration speed at small *Re* numbers obtained by Braun et al. [23] agrees with the YGB model. To include small inertial effects, the YGB model analysis was extended to the range of small *Ma* numbers [24]. For finite *Ma* numbers, several numerical simulations on the three-dimensional thermocapillary motion of non-deformable and deformable droplets were reported by Wang et al. [25] and Haj-Hariri et al. [17], respectively. They used the front-tracking and level-set methods to catch the interface and investigate the effects of physical parameters on migration speeds and mobility, respectively. For large *Ma* numbers, Balasubramanian and Subramanian [26] used thermal boundary layers and found that the migration speed of a droplet increased with increasing *Ma* number, which is in qualitative agreement with corresponding numerical simulations [27]. Both the theoretical analysis and numerical simulation are based on the assumptions of quasi-steady state and non-deformation of the droplet. However, the experimental results of Hadland et al. [11] and Xie et al. [28] were not in qualitative agreement with the above theoretical and numerical results, and it was shown that the droplet migration speed non-dimensionalized by the YGB velocity decreased as *Ma* number increased. The experiment investigation was completed in several ranges of large *Ma* numbers, where the droplet migration was in an accelerating state and did not reach a steady one. Recently, a numerical investigation based on an axisymmetric droplet model [29,30] found that the steady thermocapillary migration process did exist in a laboratory coordinate system and verified the above experimental results for the case of large *Ma* numbers, however, the effects of Capillary numbers were not given in the calculations. Owing to the invariance theory under transformation between two inertia frames, the above numerical result in a laboratory coordinate frame, i.e., the steady migration speed of the droplet decreases as *Ma* increases, should be in agreement with the theoretical and numerical results in a reference frame moving with the steady droplet velocity [26,27]. However, this seems impossible. Moreover, Herrmann et al. [18] adopted a numerical method to investigate the thermocapillary motion of deformable droplets and indicated that for large *Ma* numbers the assumption of quasi-steady state was not valid. Therefore, the thermocapillary droplet migration at large *Ma* numbers is still a topic to be studied with emphasis laid on its physical mechanism.

The planar or cylindrical droplet/bubble as a simple model has been extensively used to study its dynamical mechanism [31–33]. In this paper, we use the front-tracking method to numerically study the thermocapillary migration of a non-deformable planar droplet in the liquids at moderate and large *Ma* numbers and analyze in detail the relation of the migration velocity to the temperature distribution inside and outside the droplet. Moreover, by using asymptotic analysis, we investigate the continuity of thermal flux across the surface based on the overall energy balance of the droplet and analyze the existence of quasi-steady migration of the droplet at large *Ma* numbers.

2 Governing equations

Consider the thermocapillary migration of a planar droplet in a continuous phase fluid of infinite extent under a uniform temperature gradient G. Gravity and deformation of the droplet shape are ignored. Two-dimensional continuity, momentum and energy equations for the continuous phase fluid and the droplet in a laboratory coordinate system are written as follows:

$$\begin{aligned}
&\frac{\partial \rho_i}{\partial t} + \nabla \cdot (\rho_i \mathbf{v}_i) = 0, \\
&\frac{\partial \rho_i \mathbf{v}_i}{\partial t} + \nabla \cdot (\rho_i \mathbf{v}_i \mathbf{v}_i) = -\nabla p_i + \nabla \cdot \mu_i (\nabla \mathbf{v}_i + \nabla^T \mathbf{v}_i) + \mathbf{F}_\sigma, \\
&\frac{\partial T_i}{\partial t} + \nabla \cdot (\mathbf{v}_i T_i) = \frac{\kappa_i}{k_i} \nabla \cdot (k_i \nabla T_i),
\end{aligned} \tag{1}$$

where $\mathbf{v}_i$ and T_i are velocity and temperature, respectively. $\mathbf{F}_\sigma$ is the surface tension force acting on the interface. $\rho_i, \mu_i, k_i, \kappa_i$ represent density, dynamic viscosity, thermal conductivity, and thermal diffusivity, respectively. Symbols with subscript 1 and 2 denote physical coefficients of the continuous fluid and the droplet, respectively. The solutions of Eqs. (1) have to satisfy the boundary conditions at infinity,

$$\mathbf{v}_1 = 0, \quad T_1 \to T_0 + Gz, \tag{2}$$

where T_0 is the undisturbed temperature of the continuous phase, and the boundary conditions at the interface (r_b, z_b) of the two fluids

$$\begin{aligned} &\mathbf{v}_1(r_b, z_b, t) = \mathbf{v}_2(r_b, z_b, t), \\ &T_1(r_b, z_b, t) = T_2(r_b, z_b, t), \\ &k_1 \frac{\partial T_1}{\partial n}(r_b, z_b, t) = k_2 \frac{\partial T_2}{\partial n}(r_b, z_b, t), \end{aligned} \tag{3}$$

where $\mathbf{n}$ is a unit vector normal to the interface. In the modeling assumptions, both fluids are immiscible, and the physical properties are constant. The equations of state for density, viscosity, heat conduction, and heat diffusivity are written as follows:

$$\frac{\mathrm{d}\rho_i}{\mathrm{d}t} = \frac{\mathrm{d}\mu_i}{\mathrm{d}t} = \frac{\mathrm{d}k_i}{\mathrm{d}t} = \frac{\mathrm{d}\kappa_i}{\mathrm{d}t} = 0. \tag{4}$$

The reference velocity is defined as

$$v_o = -\sigma_T G R_0 / \mu_1, \tag{5}$$

where R_0 is the radius of the droplet, and $\sigma_T (= \mathrm{d}\sigma/\mathrm{d}T)$ is the change rate of interfacial tension with temperature. By taking R_0, v_o and GR_0 as the characteristic quantities to make coordinates, velocity and temperature dimensionless, Eqs. (1) are rewritten in the following non-dimensional form:

$$\begin{aligned} &\nabla \cdot \mathbf{v}_i = 0, \\ &\frac{\partial \rho_i \mathbf{v}_i}{\partial t} + \nabla \cdot (\rho_i \mathbf{v}_i \mathbf{v}_i) = -\nabla p_i + \frac{1}{Re} \nabla \cdot \mu_i (\nabla \mathbf{v}_i + \nabla \mathbf{v}_i^T) + \mathbf{f}_\sigma, \\ &\frac{\partial T_i}{\partial t} + \nabla \cdot (\mathbf{v}_i T_i) = \frac{1}{Ma} \frac{\kappa_i}{k_i} \nabla \cdot (k_i \nabla T_i), \end{aligned} \tag{6}$$

where the physical coefficients are non-dimensionlized by the characteristic quantities of a continuous fluid and $\mathbf{f}_\sigma = \mathbf{F}_\sigma R_0 / \rho_1 v_0^2$. The boundary conditions (2) and (3) are non-dimensionlized as

$$\mathbf{v}_1 = 0, \quad T_1 \to T_0 + z \tag{7}$$

at infinity, and

$$\begin{aligned} &\mathbf{v}_1(r_b, z_b, t) = \mathbf{v}_2(r_b, z_b, t), \\ &T_1(r_b, z_b, t) = T_2(r_b, z_b, t), \\ &k_1 \frac{\partial T_1}{\partial n}(r_b, z_b, t) = k_2 \frac{\partial T_2}{\partial n}(r_b, z_b, t) \end{aligned} \tag{8}$$

at the interface between two fluids. The Reynolds number and Marangoni number are defined as

$$Re = \frac{\rho_1 v_0 R_0}{\mu_1}, \quad Ma = \frac{v_0 R_0}{\kappa_1} = PrRe, \tag{9}$$

where $Pr = \mu_1 / \rho_1 \kappa_1$ is the Prandtl (Pr) number. In what follows, the undisturbed temperature T_0 and non-dimensional physical parameters ($\rho_1 = \mu_1 = k_1 = \kappa_1 = 1$) of the continuous phase are reduced for simplicity, except when otherwise indicated.

3 Numerical simulation of thermocapillary droplet migration at moderate and large *Ma* numbers

3.1 Models and numerical methods

As shown schematically in Fig. 1, the symmetric axis of the container is taken as the z-axis. A droplet is placed initially at the center of the coordinates and then moved along the z-axis. Thus, the solution of Eqs. (6) should satisfy the following initial conditions in the whole domain $x \in [x_0, x_1]$ and $z \in [z_0, z_1]$:

$$\mathbf{v}_i = 0, \quad T_i = z, \tag{10}$$

and non-slip/periodic boundary conditions at the top and bottom walls/the horizontal boundaries:

$$\begin{aligned} &\mathbf{v}_1(x, z_0) = \mathbf{v}_1(x, z_1) = 0, \quad T_1(x, z_0) = z_0, T_1(x, z_1) = z_1, \\ &\mathbf{v}_1(x_0, z) = \mathbf{v}_1(x_1, z), \quad T_1(x_0, z) = T_1(x_1, z). \end{aligned} \tag{11}$$

In the computation, we use a fixed regular staggered MAC grid in the computational domain. To discretize Eqs. (6), we adopt a second-order central difference scheme for the spatial variables and an explicit predictor-corrector second-order scheme for time integration. The predictor-corrector method is a combination of the explicit Euler and the implicit trapezoidal methods to obtain an explicit technique with better convergence characteristic. In the method, the solution at time step $n + 1$ is predicted by using the explicit Euler method

$$\phi^{\dagger}_{n+1} = \phi^n + f(t_n, \phi^n)\Delta t, \tag{12}$$

where † indicates that this is not the final value of the solution at t_{n+1}. Rather, the solution is corrected by applying the trapezoid rule

$$\phi^{n+1} = \phi^n + \frac{1}{2}\left[f(t_n, \phi) + f(t_{n+1}, \phi^{\dagger}_{n+1})\right]\Delta t. \tag{13}$$

To achieve the second-order accurate time integration of the velocity and temperature fields in Eqs. (6), we employ the Chorin's projection method to outline the first-order Euler integration in (12) as follows.

Since both fluids are assumed immiscible, all physical coefficients are discontinuous across the interface. The interface is captured and updated by the front-tracking method [12,13]. When the interface is moved to a new position, the density field is updated. The interface is considered to have a finite width so that the density across the interface is continuous. Here, a weighting function suggested by Peskin [34] is adopted as

$$w_{ij}(\mathbf{r}_p) = \mathrm{d}(x_p - i\Delta x)\mathrm{d}(z_p - j\Delta z) \tag{14}$$

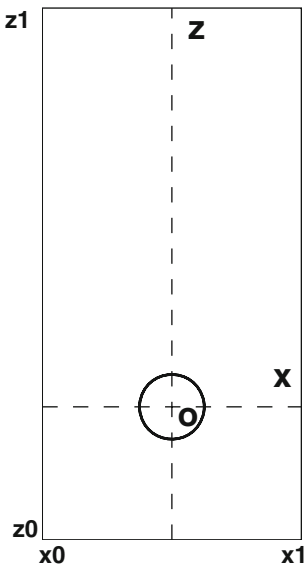

Fig. 1 Schematic of the computation domain for a planar droplet migration. The *top* and *bottom* walls are non-slip boundaries, and the *left* and *right* boundaries are periodic ones

where

$$\mathrm{d}(r) = \begin{cases} (1/4\Delta r)[1+\cos(\pi r/2h)], & |r| < 2\Delta r, \\ 0, & |r| \geq 2\Delta r, \end{cases} \tag{15}$$

and (x_p, z_p) is the interface node. Once the density is updated, the velocity field will be computed by Chorin's projection method, which is divided into two steps. One is a prediction step, where the effect of the pressure is ignored,

$$\frac{\rho_i^{n+1}\mathbf{v}_i^* - \rho_i^n \mathbf{v}_i^n}{\Delta t} = -\nabla\cdot(\rho_i^n \mathbf{v}_i^n \mathbf{v}_i^n) + \frac{1}{Re}\nabla\cdot\mu_i^n(\nabla\mathbf{v}_i^n + \nabla^T\mathbf{v}_i^n) + \mathbf{f}_\sigma. \tag{16}$$

Another is a correction step in terms of the pressure gradient,

$$\frac{\rho_i^{n+1}\mathbf{v}_i^{n+1} - \rho_i^{n+1}\mathbf{v}_i^*}{\Delta t} = -\nabla p_i^{n+1}, \tag{17}$$

where the pressure is obtained by solving the following Poisson equation:

$$\nabla\cdot\frac{1}{\rho_i^{n+1}}\nabla p_i^{n+1} = \frac{1}{\Delta t}\nabla\cdot\mathbf{v}_i^*. \tag{18}$$

In solving Eq. (18), we use the successive over relaxation iteration method to get p_i^{n+1}. When the pressure is obtained, the corrected velocity field $\mathbf{v}_i^{n+1}$ is determined from Eq. (17). Similarly, the energy equation is discretized in the form

$$\frac{T_i^{n+1} - T_i^n}{\Delta t} = -\nabla\cdot(\mathbf{v}_i^{n+1}T_i^n) + \frac{1}{Ma}\frac{\kappa_i^n}{k_i^n}\nabla\cdot(k_i^n\nabla T_i^n). \tag{19}$$

In terms of the corrected velocity field $\mathbf{v}_i^{n+1}$, the temperature field T_i^{n+1} is determined. Until now, by using the projection method, the first-order time integration $\phi_{n+1}^\dagger$ of the velocity, pressure, and temperature fields is completed. In the mean time, other physical coefficients (μ, k, κ) across the interface at the time step $n+1$ are also updated to have the same distribution as the density. Repeating the above process, we get a second first-order accurate solution $\phi_{n+2}^{\dagger\dagger}$ at time step $n+2$ based on the first-order accurate solution $\phi_{n+1}^\dagger$,

$$\phi_{n+2}^{\dagger\dagger} = \phi_{n+1}^\dagger + f\left(t_{n+1}, \phi_{n+1}^\dagger\right)\Delta t. \tag{20}$$

Finally, the solution for the second-order time integration is obtained as follows:

$$\phi^{n+1} = \left(\phi^n + \phi_{n+2}^{\dagger\dagger}\right)/2. \tag{21}$$

Since the droplet in the migration process is assumed non-deformable, the vertical area average velocity in the droplet is taken as the droplet migration velocity V_z. The nodes of interface are moved with this velocity at each time step.

In solving Eq. (16), the surface tension force $\mathbf{f}_\sigma$ is determined by referring to the temperature field. In general, the surface tension force on a short front element is defined as

$$\delta\mathbf{F}_\sigma = \int_{\Delta s}\frac{\partial}{\partial s}(\sigma\mathbf{t})\mathrm{d}s = (\sigma\mathbf{t})_2 - (\sigma\mathbf{t})_1 = \Delta_{21}(\sigma\mathbf{t}), \tag{22}$$

where $\mathbf{t}$ is a unit tangent vector, s is the arc length along the interface. σ is the surface tension coefficient written as

$$\sigma = \sigma_0 + \sigma_T T, \tag{23}$$

where σ_0 is the surface tension coefficient at a reference temperature T_0, and σ_T is a negative constant for most fluids. By using the above characteristic quantities, the non-dimensional surface tension force is written in the form of body force as

$$\begin{aligned}\delta\mathbf{f}_\sigma &= \delta\mathbf{F}_\sigma(R_0/\rho_1 v_0^2)/(R_0^2\delta x\delta z),\\ &= \Delta_{21}(\sigma\mathbf{t})/\rho_1 v_0^2 R_0\delta x\delta z,\\ &= \Delta_{21}[(\sigma_0/v_0\mu_1 - T)\mathbf{t}]/Re\delta x\delta z,\\ &= \Delta_{21}[(1/Ca - T)\mathbf{t}]/Re\delta x\delta z,\end{aligned} \tag{24}$$

where $Ca(=v_0\mu_1/\sigma_0)$ is the Capillary number. To calculate the surface tension force $\mathbf{f}_\sigma$, the surface temperature on the interface is firstly obtained by interpolating values on the grid points. The tangent vector is computed from a Lagrangian interpolation polynomial fitting through four interface nodes. Then, the surface tension force on the interface is distributed to the grid points by means of the weighting function (14).

3.2 Results and analysis

To check the sensitivity of the results to grid refinements, we perform calculations for a planar droplet migration at $Re = 5$, $Ma = 20$, $Ca = 0.01666$ and $\rho_2 = \mu_2 = k_2 = \kappa_2 = 0.5$ using the method described above. The computational domain is chosen as 4×8. Based on 64×128, 96×192, and 128×256 grid points, i.e., 16, 24, and 32 grid points per droplet radius, the time evolution of the droplet migration velocity is calculated and plotted in Fig. 2. The migration velocity curve seems to converge when the grid becomes finer. The difference in the migration velocities computed with 24 and 32 grid points per droplet radius is very small (about 1.5%). In the following calculations, we fix 24 grid points per droplet radius as the grid resolution. To further validate our code, we compare the current computation results with Nas and Tryggvason's [15], where the deformation of the droplet is considered. In Fig. 3, it is observed that both results have the same trends and the migration velocities are close together.

In the following calculations, we adopt the silicone oil of nominal viscosity 5cst and the FC-75 Fluorinert liquid, i.e., the working media in the space experiment [28], as the continuous phase fluid and the droplet, respectively. The physical parameters of the continuous fluid and the droplet at temperature 25°C are given in Table 1. σ_T is fixed as -0.044 dyn/cmK [28], and $\sigma_0 \approx 6$ dyn/cm [35] is adopted. From the values of the continuous fluid parameters, the Pr number and the capillary length $\lambda_0 = \sqrt{\sigma_0/\rho_1 g_0}$ (with the earth's gravity $g_0 = 980$ cm/s^2) are determined as 67.8 and 0.08 cm, respectively. Most of the droplets in the space experiment [28] have $R_0 \geq \lambda_0$, which refers to the domination of the gravitational effect to the droplet shapes

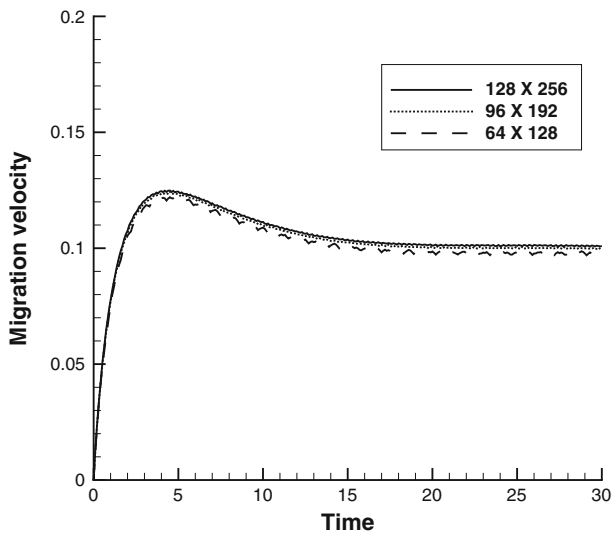

Fig. 2 Droplet migration velocity versus non-dimensional time for three grid resolutions 64×128, 96×192, and 128×256 at a fixed domain 4×8 under $Re = 5$, $Ma = 20$, $Ca = 0.01666$ and $\rho_2/\rho_1 = \mu_2/\mu_1 = k_2/k_1 = \kappa_2/\kappa_1 = 0.5$

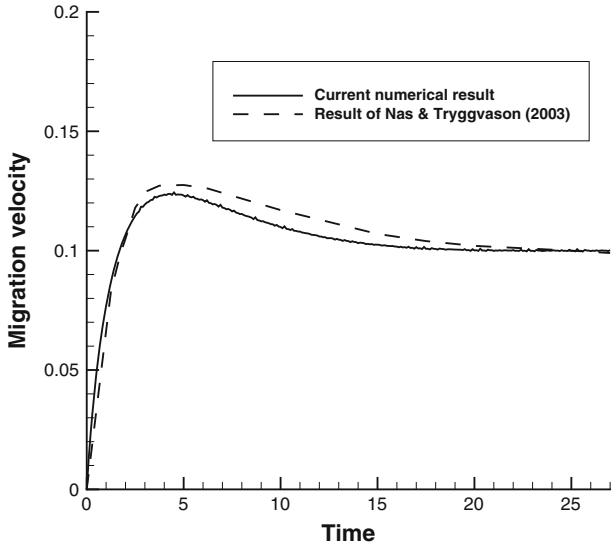

Fig. 3 Time evolution of the droplet migration velocity for grid resolution 96×192 and its comparison with Nas and Tryggvason's result [15] for the same parameters as given in Fig. 2

Table 1 Physical parameters of the continuous fluid (5cst silicone oil) and the droplet (FC-75) at temperature 25°C, which are the working media in the space experiment [28]

	ρ (g/cm^3)	μ (10^{-2}dyns/cm^2)	k (W/mK)	κ (10^{-4}cm^2/s)
Silicone oil	0.91	4.268	0.111	6.915
FC-75	1.77	1.416	0.063	2.018

on the earth. However, in the microgravity environment(the effective gravity g_e is about $O(10^{-6})$ of g_0), the gravitational effect is neglected($R_0 \ll \lambda_e$), so the droplet shapes are dominated by the capillary effect. The computational domain is chosen as $\{x, z\} \in \{[-4, 4], [-4, 16]\}$ and the resolution is fixed at 192×480. The initial droplet is placed at the position (0,0), and the time step is 0.0002.

3.2.1 Flow field with the temperature gradient $G = 12$ K/cm

In the space experiments with $G = 12$ K/cm [28], Re and Ma lie, respectively, in the ranges of 4.5–302.6 and 145–5,525, their specific values depending on R_0. To simulate the experimental processes, the physical coefficients in the droplet migration processes are determined by changing R_0. The correspondence of Re, Ma, and Ca to R_0 is presented in Table 2, where Re is in a range of moderate values and Ma have both moderate and large numbers. Figure 4 displays the time evolution of droplet migration velocities for five sets of non-dimensional coefficients. In the present range of Ma, the migration velocities versus time have complex behaviors, which can be classified into three types based on the curve characters. At $Ma = 44.7$ ($Re = 0.66$), the initial migration velocity increases sharply before $t = 3$ and then drops to approach a steady value. For $Ma = 402.5$–1118.1($Re = 5.93$–16.5), the initial accelerating process has a smaller peak value as Ma increases. After the increasing–decreasing oscillation process, the terminal droplet migration velocity increases with time,

Table 2 Correspondence of non-dimensional parameters Re, Ma, and Ca to the droplet radius R_0 for the droplet migration in a flow field with the temperature gradient $G = 12$ K/cm

R_0(cm)	Re	Ma	Ca
0.05	0.66	44.7	0.0044
0.15	5.93	402.5	0.013
0.25	16.5	1118.1	0.022
0.35	32.3	2191.6	0.031
0.45	53.4	3622.8	0.040

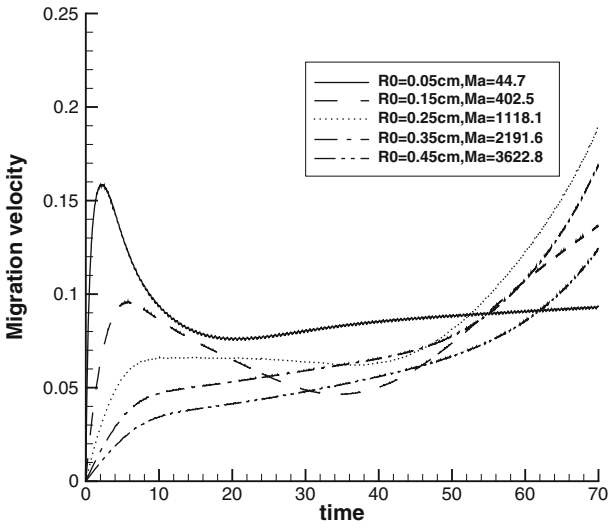

Fig. 4 Droplet migration velocity in a flow field with the temperature gradient $G = 12$ K/cm versus non-dimensional time at $Ma = 44.7$, 402.5, 1,118.1, 2,191.6, and 3,622.8

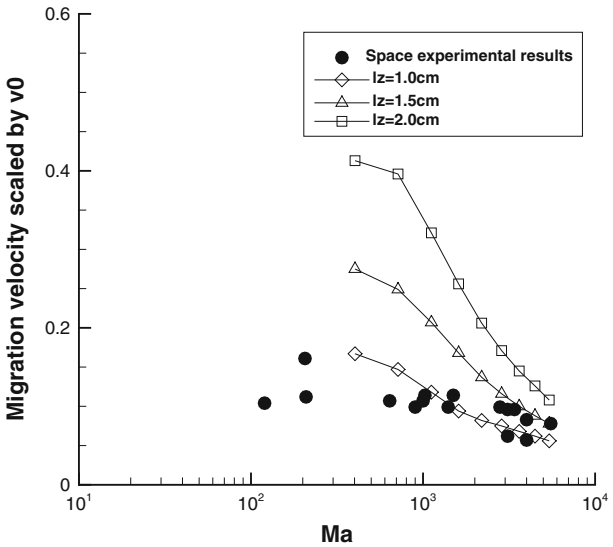

Fig. 5 Instantaneous thermocapillary migration velocity of the droplet in a flow field with the temperature gradient $G = 12$ K/cm at a fixed migration distance $l_z = 1/1.5/2$ cm denoted by *diamonds*/*deltas*/*squares* versus *large Ma numbers*. The experimental results [28] rescaled by $V_{YGB}/v_0 = 2/[(2 + 3\mu_2/\mu_1)(2 + k_2/k_1)]$ are plotted and denoted by *circles*

i.e., the droplet migration is in an accelerating state. The slope of the curve increases as *Ma* increases. For $Ma = 2191.6$–3622.8 ($Re = 32.3$–53.4), the droplet migration velocity increases monotonously with time and decreases with increasing *Ma*. We can thus conclude that in the time frame under investigation the thermocapillary droplet migration is steady at moderate *Ma* numbers, but becomes unsteady at large *Ma* numbers. In the two space experiments, Figs. 4 of [11] and [28] showed that the whole migration processes were unsteady and did not reach any steady state. Even a plateau appears in the curve of migration velocity vs migration distance, the migration process seems to be an accelerating one after the slow varying period. To further compare with the experimental investigation [28], we take several fixed migration distances l_z and determine the relation between instantaneous non-dimensional migration velocity V_z and *Ma* numbers. The numerical and experimental results are plotted in Fig. 5, from which it is evident that both the numerical and experimental migration velocities of droplet decrease as *Ma* increases in the range of large *Ma* numbers. Hence, at large *Ma* numbers, the above simulation results are in qualitative agreement with those of experimental investigations [11,28].

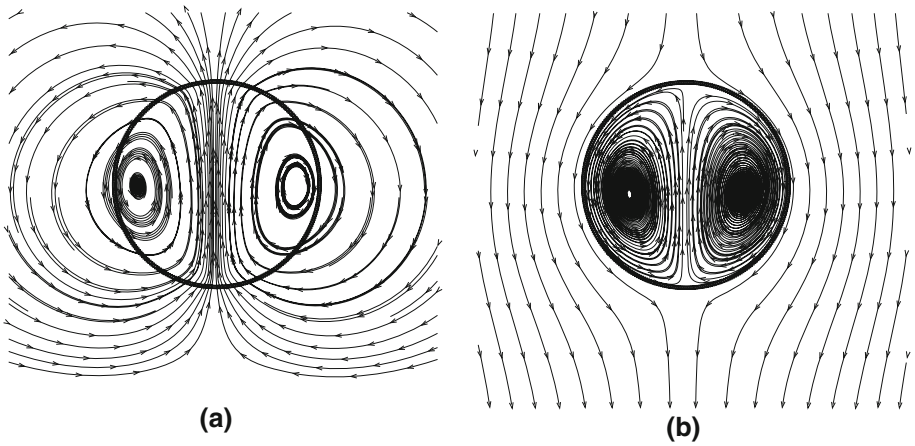

Fig. 6 Computed velocity fields at $t = 20$ under $R_0 = 0.25$ cm, $Re = 16.5$, $Ma = 1{,}118.1$ in (**a**) the laboratory coordinate frame and (**b**) the reference frame moving with the droplet

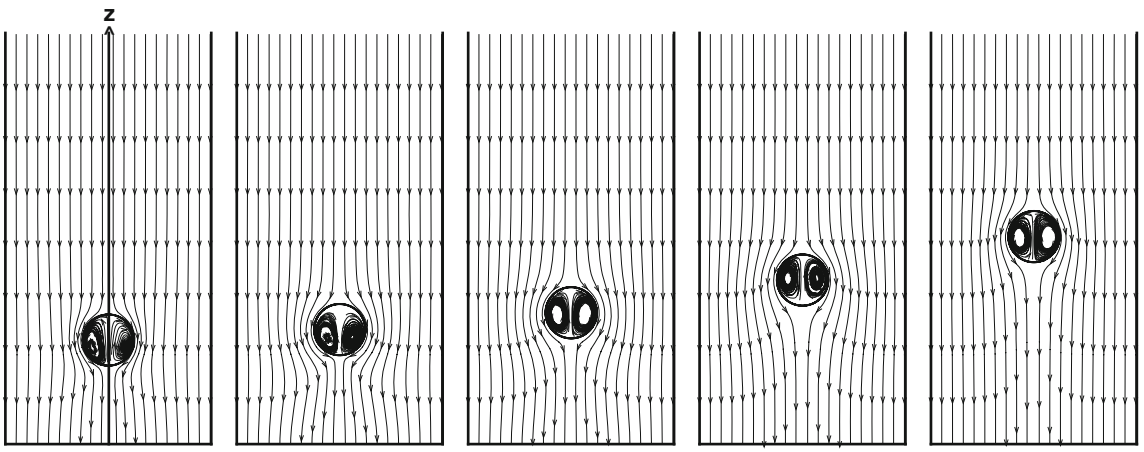

Fig. 7 Streamlines in a reference frame moving with the droplet under $R_0 = 0.25$ cm, $Re = 16.5$, $Ma = 1{,}118.1$. Their time evolution is displayed in *5 small figures* from *left* to *right*. The non-dimensional time is chosen as 3, 10, 20, 40, and 60, respectively

In order to understand the phenomena exhibited in droplet migration processes, it is important to analyze the evolution of the velocity and temperature fields. Figure 6 displays the computed velocity fields at $t = 20$ in both the laboratory coordinate frame and the reference frame moving with the droplet at $Re = 16.5$ ($Ma = 1{,}118.1$). In the laboratory coordinate frame, the streamlines for a moving droplet are closed and symmetric about the z-axis. In the reference frame, when the external streamlines go around the droplet, a pair of vortices is formed inside the droplet. It is evident that in the reference frame recirculation flows in both the continuous phase fluid and the droplet are driven by the surface tension force generated by the temperature gradient along the surface. In Fig. 7, we depict the pattern evolution of streamlines with time in a reference frame moving with the droplet at $Re = 16.5$ ($Ma = 1{,}118.1$). Initially, there appear two vortices symmetric about the vertical diameter. Along with the rising of the droplet, the pair of vortices in the droplet is kept, but the vortex centers are moving up. In the whole process, the basic types of streamlines for both the internal and external motions are not changed. For moderate Re numbers, both the convection and viscous terms in the momentum equation have important effects on the fluid flow. The external flow just passes around the droplet and does not separate from the droplet surface, and thus the computed velocity fields are similar in the range of moderate Re numbers.

In the range of R_0, the fluid flow has behaviors similar to those for moderate Re numbers, but the thermal transfer exhibits different characters for moderate and large Ma numbers. For moderate Ma numbers, both the heat convection and the heat conduction have important effects on the energy transfer. Figure 8 displays the time evolution of isotherms at moderate Ma ($Ma = 44.7$, $Re = 0.66$), which corresponds to that of migration velocities shown in Fig. 4. As given in Eq. (23), the surface tension coefficient decreases with the increasing of the local temperature. For a temperature field with its gradient in the z direction, the generated surface

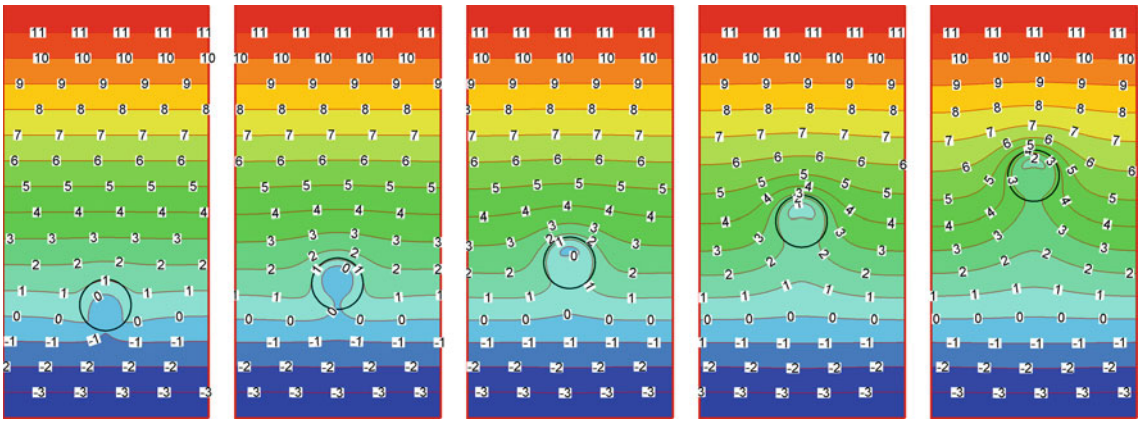

Fig. 8 Isotherms in a laboratory coordinate frame are selected from the computation of the droplet migration under $R_0 = 0.05$ cm, $Re = 0.66$, $Ma = 44.7$. Notation is the same as in Fig. 7

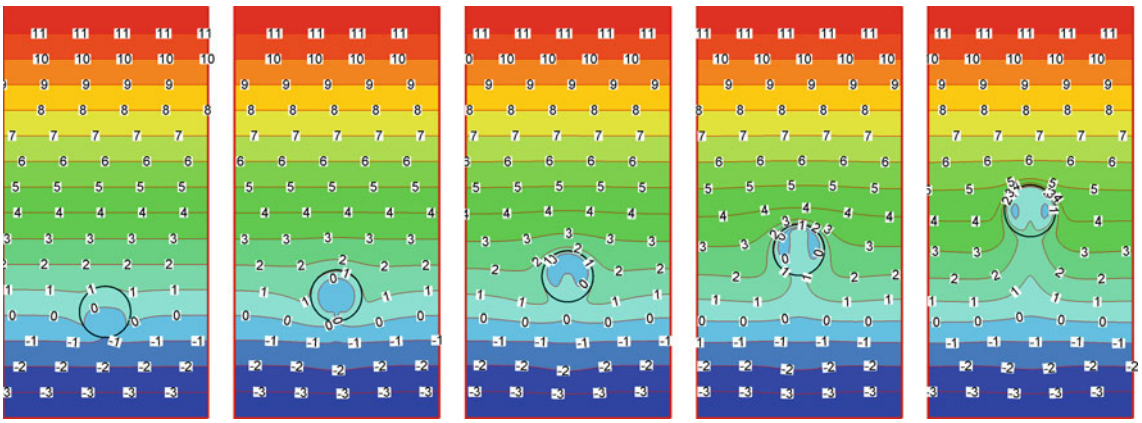

Fig. 9 Same as Fig. 8, except $R_0 = 0.15$ cm, $Re = 5.93$, $Ma = 402.5$

tension force is a net force along the surface. At the beginning, the droplet starts to move toward the warm side under the action of net force. It induces in turn viscous stresses in both fluids, which causes streamlines inside and outside the droplet to form double vortices and to go around the droplet, respectively. The temperature field inside the droplet is affected by the two rotating vortices. The horizontal isotherm $T = 0$ in the droplet is moving up, as well as bending along the migration direction. Along with the rising of the droplet, both the internal and external temperature fields around the droplet surface are re-distributed due to the action of heat convection. In the process, the isotherm $T = 0$ moves up and approaches the top of the droplet. At $t = 20$, a small cap-type isotherm $T = 0$ is formed within the droplet. Meanwhile, under the action of heat conduction, the thermal energy is transferred from outside of the droplet to inside, so the temperature inside the droplet increases. At $t = 60$, the temperature of cap-type isotherm in the droplet reaches $T = 2$. Hence, both the temperature fields inside and outside the droplet increase with time. Only when both the internal and external temperature fields satisfy linear relations with the same slope does the droplet migration reach a steady state. For large Ma numbers, the effect of heat convection is stronger than that of heat conduction. Figure 9 displays the time evolution of isotherms at large Ma ($Ma = 402.5$, $Re = 5.93$), which corresponds to that of the migration velocity shown in Fig. 4. In the initial (accelerating) stage of migration, the evolution of the isotherms is similar to that shown in Fig. 8. In the following (oscillation) stage of migration, the bent isotherms in the droplet move to approach the top of the droplet and are converted to pea-type ones and then to earphone-type ones. In the last (accelerating) stage of migration, the earphone-type isotherms are transformed into those with two symmetric vortices. In the whole migration process, although the temperature inside the droplet increases, the temperature of minimal isotherm is still kept at $T = 0$. It implies that the thermal energy transfer from outside of the droplet to inside is weaker than that shown in Fig. 8. Figure 10 displays the time evolution of isotherms at a still larger Ma ($Ma = 2{,}191.6$, $Re = 32.3$), which corresponds to that of the migration

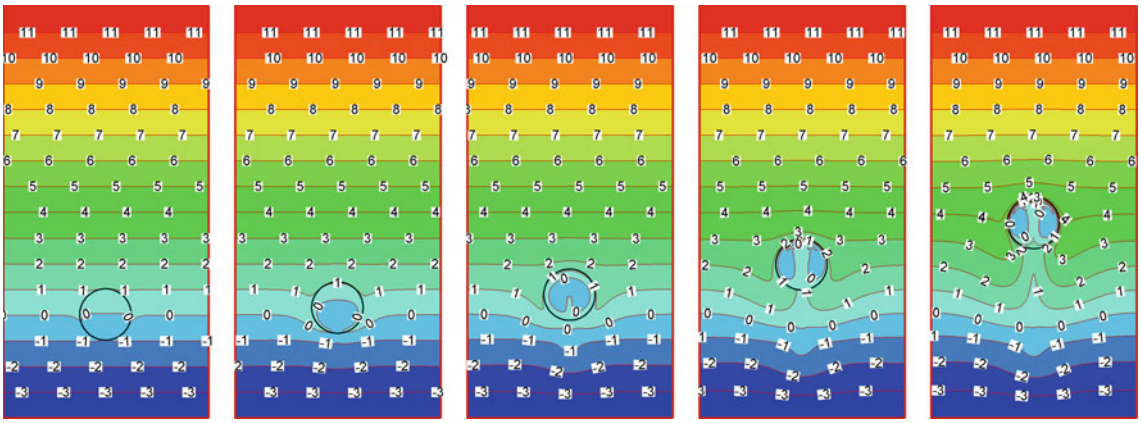

Fig. 10 Same as Fig. 8, except $R_0 = 0.35$ cm, $Re = 32.3$, $Ma = 2{,}191.6$

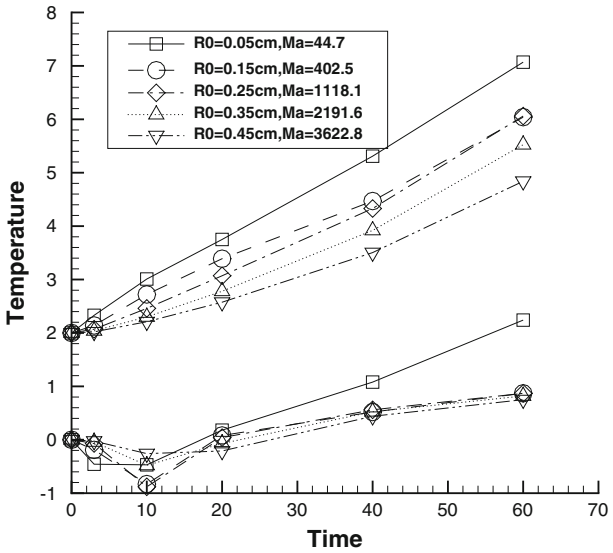

Fig. 11 Time evolution of temperature at point (x_c, z_c) inside the droplet and point $(x_c, z_c + 2)$ outside the droplet, where (x_c, z_c) is the center of the droplet in the laboratory coordinate system

velocity shown in Fig. 4. In the whole (accelerating) process of migration, the initial evolution of the isotherms is similar to that shown in Fig. 9, except for the slower movement of the isotherms in approaching the top of the droplet. Then, the pea-type isotherms are converted to earphone-type ones. And finally, the isotherms with two vortices symmetric about the vertical diameter in the droplet are formed. At $t = 60$, the fact that the minimal isotherm $T = 0$ has larger closed area in the droplet means that the thermal energy transfer from outside of the droplet to inside is weaker than that shown in Fig. 9. Thus, at large Ma numbers, although the temperature outside the droplet increases fast as the droplet rises, the temperature inside the droplet has only a slow increase. The droplet migration does not reach a steady state and is thus an unsteady process.

To further quantitatively depict the steady and unsteady migration processes, we will investigate the time evolution of temperature fields inside and outside the droplet. Figure 11 displays the temperature at the point (x_c, z_c) inside the droplet and the point $(x_c, z_c + 2)$ outside the droplet in the migration processes, where (x_c, z_c) is the center of the droplet in the laboratory coordinate system. It is evident that for the moderate Ma(=44.9) number time evolution curves of the temperature at these two points after $t_0 = 20$ are approximately linear and parallel. Both the temperatures inside and outside the droplet satisfy the linear relation: $T_i = T_i(t_0) + V_\infty(t - t_0)$, which indicates a steady migration process with the constant velocity $V_z = V_\infty$. However, for large Ma numbers, although the time evolution curves of the temperature inside and outside the droplet after $t_0 = 20$ are approximately linear, they are not parallel. The slope of the time evolution curve of the temperature inside the droplet is smaller than that outside the droplet, so the difference of the temperatures

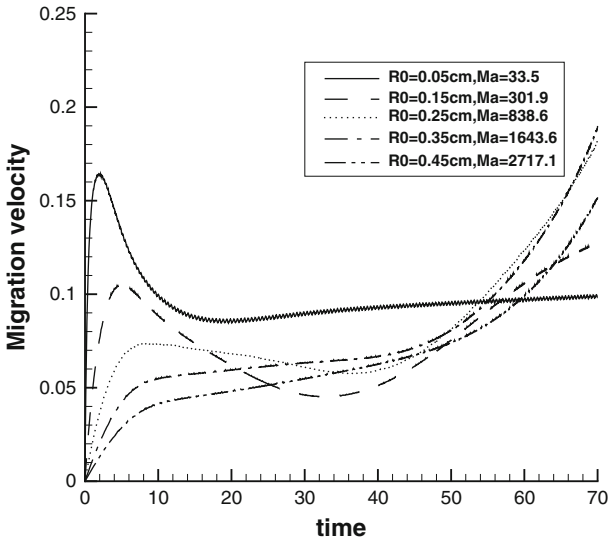

Fig. 12 Droplet migration velocity in a flow field with the temperature gradient $G = 9$ K/cm versus non-dimensional time at $Ma = 44.7$, 301.9, 838.6, 1,643.7, and 2,717.1

at these two points increases as time increases. It implies that the terminal droplet migration does not reach a steady state and is thus an unsteady process. Therefore, the advection around the droplet is a more significant mechanism for heat transfer across/around the droplet at large *Ma* numbers.

3.2.2 Flow field with the temperature gradient G = 9 K/cm

In the space experiments with $G = 9$ K/cm [28], *Re* and *Ma* lie, respectively, in the ranges of 3.2–89.8 and 148–4,103, their specific values depending on R_0. To simulate the experimental processes, the physical coefficients in the droplet migration processes are determined by changing R_0. The correspondence of *Re*, *Ma* and *Ca* to R_0 is presented in Table 3, where *Re* is in a range of moderate values and *Ma* have both moderate and large numbers. Figure 12 displays the time evolution of droplet migration velocities for five sets of non-dimensional coefficients. In the present range of *Ma*, the curves of migration velocities versus time are classified into three types based on their characters. At $Ma = 33.5$ ($Re = 0.49$), the initial migration velocity increases sharply near $t = 2$ and then drops to approach a steady value. For $Ma = 301.9$–838.6 ($Re = 4.45$–12.4), after the increasing–decreasing oscillation process, the droplet migration is in an accelerating state. For $Ma = 1{,}643.6$–$2{,}717.1$ ($Re = 24.2$–40.1), the droplet migration velocity increases monotonously with time and decreases with increasing *Ma*. We can thus conclude that in the time frame under investigation the thermocapillary droplet migration is steady at moderate *Ma* numbers, but becomes unsteady at large *Ma* numbers. To further compare with the experimental investigation [28], we take several fixed migration distances l_z and determine the relation between instantaneous non-dimensional migration velocity V_z and *Ma* numbers. The numerical and experimental results are plotted in Fig. 13, from which it is evident that both the numerical and experimental migration velocities of the droplet decrease as *Ma* increases in the range of large Ma numbers. Hence, at large *Ma* numbers, the above simulation results are in qualitative agreement with those of experimental investigations.

Table 3 Correspondence of non-dimensional parameters *Re*, *Ma*, and *Ca* to the droplet radius R_0 for the droplet migration in a flow field with the temperature gradient $G = 9$ K/cm

R_0(cm)	*Re*	*Ma*	*Ca*
0.05	0.49	33.5	0.0033
0.15	4.45	301.9	0.010
0.25	12.4	838.6	0.017
0.35	24.2	1,643.6	0.023
0.45	40.1	2,717.1	0.030

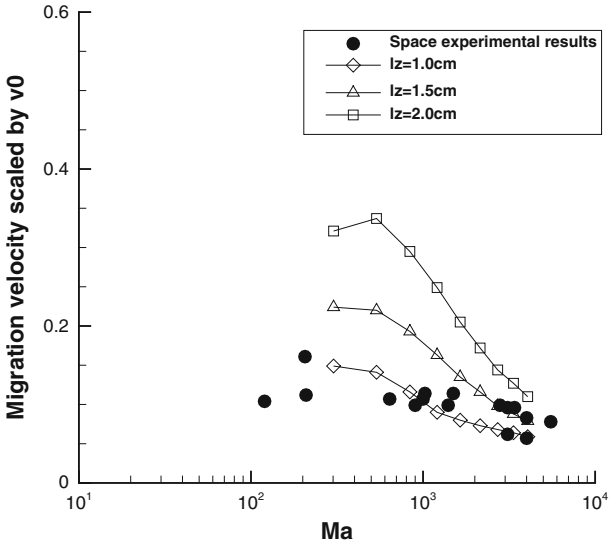

Fig. 13 Instantaneous thermocapillary migration velocity of the droplet in a flow field with the temperature gradient $G = 9\,\mathrm{K/cm}$ at a fixed migration distance $l_z = 1/1.5/2$ cm denoted by *diamonds*/*deltas*/*squares* versus *large Ma numbers*. The experimental results [28] rescaled by $V_{YGB}/v_0 = 2/[(2+3\mu_2/\mu_1)(2+k_2/k_1)]$ are plotted and denoted by *circles*

4 Theoretical analysis of thermocapillary droplet migration at large *Ma* numbers

4.1 Quasi-steady-state assumption

In general, the surface tension is a linear decreasing function of the local temperature. For a temperature field with its gradient in the z direction, the generated surface tension force is a net force along the surface, and the droplet starts to move toward the warm side under the action of net force. When the net force acting on the droplet at the flow direction is zero, the thermocapillary droplet migration reaches a steady process. However, due to the variation of physical parameters with the ambient temperature, the migration process may not reach any steady state. Only when the migration is sufficiently slow that the order of relevant time scale for the transport process to generate steady velocity and temperature fields is smaller than that for the droplet to move an appreciable distance, the assumption of the quasi-steady state is valid. It means that after experiencing an initial unstable migration process the droplet migration may reach a steady state at the time t_0 and the position $\mathbf{r}_0 = z_0\mathbf{k}$, i.e., migrating with a constant droplet migration speed V_∞. Using the coordinate transformation from the laboratory coordinate system to a coordinate system moving with the droplet velocity V_∞,

$$\begin{aligned} \mathbf{r} &= \bar{\mathbf{r}} + \mathbf{r}_0 + V_\infty(t - t_0)\mathbf{k}, \\ \mathbf{v}_i(\mathbf{r}, t) &= \bar{\mathbf{v}}_i(\bar{\mathbf{r}}) + V_\infty\mathbf{k}, \\ T_i(\mathbf{r}, t) &= \bar{T}_i(\bar{\mathbf{r}}) + z_0 + V_\infty(t - t_0), \end{aligned} \tag{25}$$

the energy equation in Eqs. (6) can be formulated as

$$V_\infty + \bar{\nabla}\cdot(\bar{\mathbf{v}}_i\bar{T}_i) = \frac{1}{Ma}\frac{\kappa_i}{k_i}\bar{\nabla}\cdot(k_i\bar{\nabla}\bar{T}_i) \tag{26}$$

in a polar coordinate system $\bar{\mathbf{r}} = (\bar{r}, \theta)$. Under the assumption of a non-deformable droplet, the radial coordinate axis is the outer normal vector of the interface. By using the transformation (25), the boundary conditions (7) and (8) can be, respectively, written as follows:

$$\bar{\mathbf{v}}_1 = -V_\infty\mathbf{k},\ \bar{T}_1 \to \bar{r}\cos\theta, \tag{27}$$

at places far away from the droplet and

$$\begin{aligned} \bar{u}_{1n}(1,\theta) &= \bar{u}_{2n}(1,\theta) = 0, \\ \bar{v}_{1s}(1,\theta) &= \bar{v}_{2s}(1,\theta), \\ \bar{T}_1(1,\theta) &= \bar{T}_2(1,\theta), \\ \frac{\partial \bar{T}_1}{\partial n}(1,\theta) &= k_2 \frac{\partial \bar{T}_2}{\partial n}(1,\theta) \end{aligned} \tag{28}$$

at the interface of the two fluids. Thus, once the droplet migration reaches a steady state, the above problem of (6, 7, 8) in the laboratory coordinate system can be described by steady energy equations (26) with boundary conditions (27, 28) in the coordinate system moving with the droplet velocity. This implies the overall steady-state energy balance with two phases in the flow domain in the co-moving frame of reference.

4.2 Non-conservative integral thermal flux across the droplet surface at large *Ma* numbers

To analyze the energy equations with a small parameter $\epsilon = 1/\sqrt{V_\infty Ma}$, Eqs. (26) are rewritten as

$$1 + \bar{\nabla} \cdot (\bar{\mathbf{v}}_1 \bar{T}_1) = \epsilon^2 \bar{\nabla} \cdot (\bar{\nabla} \bar{T}_1), \tag{29}$$

$$1 + \bar{\nabla} \cdot (\bar{\mathbf{v}}_2 \bar{T}_2) = \epsilon^2 \kappa_2 \bar{\nabla} \cdot (\bar{\nabla} \bar{T}_2), \tag{30}$$

where both the velocity fields $\bar{\mathbf{v}}_i$ in the surrounding fluids and in the droplet are rescaled by V_∞.

To confirm the overall steady-state energy balance of two phases in the flow domain with respect to the co-moving frame of reference, we have to integrate Eqs. (29, 30) with an asymptotic expansion of the outer temperature field at infinity with respect to the small parameter ϵ. To determine the asymptotic behavior of $\bar{T}_1$ at $\bar{r} \gg 1$, we rewrite Eq. (29) as follows:

$$1 + \bar{u}_1 \frac{\partial \bar{T}_1}{\partial \bar{r}} + \frac{\bar{v}_1}{\bar{r}} \frac{\partial \bar{T}_1}{\partial \theta} = \epsilon^2 \bar{\Delta} \bar{T}_1. \tag{31}$$

Letting

$$\begin{aligned} \bar{u}_1 &= \bar{u}_1^0 + o(1), \\ \bar{v}_1 &= \bar{v}_1^0 + o(1), \\ \bar{T}_1 &= \bar{T}_1^0 + o(1), \end{aligned} \tag{32}$$

we have the energy equation to leading order

$$1 + \bar{u}_1^0 \frac{\partial \bar{T}_1^0}{\partial \bar{r}} + \frac{\bar{v}_1^0}{\bar{r}} \frac{\partial \bar{T}_1^0}{\partial \theta} = 0. \tag{33}$$

By using the characteristic line method, the primary approximation of the outer temperature field in the continuous phase is derived as

$$\bar{T}_1 = \bar{r} \cos\theta + \int_\infty^{\bar{r}} (\bar{v}_1^0 \sin\theta - \bar{u}_1^0 \cos\theta - 1)/\bar{u}_1^0|_\Psi \mathrm{d}\tilde{r} + o(1), \tag{34}$$

where $\Psi \sim (\bar{r} - 1/\bar{r}) \sin\theta$. For moderate *Re* numbers, the velocity fields in Eq. (34) can be described by the potential flows. By using the scaled inviscid velocity field in the continuous phase flow passing a circular cylinder [36]

$$\begin{aligned} \bar{u}_1^0 &= -\cos\theta \left(1 - \frac{1}{\bar{r}^2}\right), \\ \bar{v}_1^0 &= \sin\theta \left(1 + \frac{1}{\bar{r}^2}\right), \end{aligned} \tag{35}$$

Eq. (34) is written as

$$\bar{T}_1 = \bar{r}\cos\theta + \int_{\bar{r}}^{\infty} \frac{1}{\tilde{r}^2 - 1} \frac{2\Psi^2/(\tilde{r} - 1/\tilde{r})^2 - 1}{\pm\sqrt{1 - \Psi^2/(\tilde{r} - 1/\tilde{r})^2}} |_{\Psi} \mathrm{d}\tilde{r} + o(1), \tag{36}$$

where $\Psi[= \sin\theta(\bar{r} - 1/\bar{r})]$ is the streamfunction of the continuous phase, the symbol "+" before the integral is so determined as to preserve the monotonously increasing trend of $\bar{T}_1(\bar{r}, 0)$ with $\bar{r}(>1)$ in the continuous phase, and the symbol "±" in the integral depends on the value of θ (the symbol "+"/"−" corresponds to $\theta \in [0, \pi/2)/[\pi/2, \pi)$). At $\bar{r} \gg 1$, Eq. (36) can be expressed as

$$\begin{aligned} \bar{T}_1 &\approx \bar{r}\cos\theta + \int_{\bar{r}}^{\infty} \frac{1}{\tilde{r}^2} \frac{2\Psi^2/\tilde{r}^2 - 1}{\pm\sqrt{1 - \Psi^2/\tilde{r}^2}} |_{\Psi} \mathrm{d}\tilde{r} + o(1) \\ &= \bar{r}\cos\theta - \frac{1}{\bar{r}}\cos\theta + o(1), \end{aligned} \tag{37}$$

where $\Psi \approx \sin\theta\bar{r}$.

In physics, the thermocapillary migration of a planar droplet has the mirror symmetry about the coordinate axis $\theta = 0$ or π, so the overall energy balance in the whole flow domain $\theta \in [0, 2\pi)$ can be generated by combining the energy balance in two connected flow domains $\theta \in [0, \pi)$ and $\hat{\theta} \in [0, \pi)$ through the transformation $\hat{\theta} = 2\pi - \theta$. Integrating Eqs. (29, 30) in the continuous phase domain ($\bar{r} \in [1, \bar{r}_\infty], \theta \in [0, 2\pi]$) and within the droplet region ($\bar{r} \in [0, 1], \theta \in [0, 2\pi]$) and then transforming them to linear integration on the droplet surface and the surface at infinity by using Green's formula, we have

$$\pi(\bar{r}_\infty^2 - 1) + \oint \bar{u}_{1n}\bar{T}_1|_{\bar{r}_\infty} \mathrm{d}s - \oint \bar{u}_{1n}\bar{T}_1|_1 \mathrm{d}s = \epsilon^2 \left(\oint \frac{\partial \bar{T}_1}{\partial n}|_{\bar{r}_\infty} \mathrm{d}s - \oint \frac{\partial \bar{T}_1}{\partial n}|_1 \mathrm{d}s \right) \tag{38}$$

and

$$\pi + \oint \bar{u}_{2n}\bar{T}_2|_1 \mathrm{d}s = \epsilon^2\kappa_2 \oint \frac{\partial \bar{T}_2}{\partial n}|_1 \mathrm{d}s. \tag{39}$$

Using the normal velocity boundary condition at the interface in (28) and the temperature field at infinity in (37), we can derive

$$\oint \frac{\partial \bar{T}_1}{\partial n}|_1 \mathrm{d}s = -\frac{\pi}{\epsilon^2}\left(1 - \frac{1}{\bar{r}_\infty^2}\right) + o\left(\frac{1}{\epsilon^2}\right) \approx -\frac{\pi}{\epsilon^2} \tag{40}$$

and

$$\oint \frac{\partial \bar{T}_2}{\partial n}|_1 \mathrm{d}s = \frac{\pi}{\kappa_2\epsilon^2}. \tag{41}$$

To analyze the thermal flux near the boundary, we write the integrals of Eqs. (40, 41) in their discretization forms and simplify the expressions in terms of the mirror symmetrical relationship $\frac{\partial \bar{T}_i}{\partial \bar{r}}|_{1,\theta} = \frac{\partial \bar{T}_i}{\partial \bar{r}}|_{1,2\pi-\theta}$ as

$$\oint \frac{\partial \bar{T}_1}{\partial n}|_1 \mathrm{d}s = \int_0^{2\pi} \frac{\partial \bar{T}_1}{\partial \bar{r}}|_1 \mathrm{d}\theta = \sum_{i=1}^{N} \frac{\partial \bar{T}_1}{\partial \bar{r}}|_1 \Delta\theta = 2\sum_{i=1}^{N/2} \frac{\partial \bar{T}_1}{\partial \bar{r}}|_1 \Delta\theta < 0 \tag{42}$$

and

$$\oint \frac{\partial \bar{T}_2}{\partial n}|_1 \mathrm{d}s = \int_0^{2\pi} \frac{\partial \bar{T}_2}{\partial \bar{r}}|_1 \mathrm{d}\theta = \sum_{i=1}^{N} \frac{\partial \bar{T}_2}{\partial \bar{r}}|_1 \Delta\theta = 2\sum_{i=1}^{N/2} \frac{\partial \bar{T}_2}{\partial \bar{r}}|_1 \Delta\theta > 0, \tag{43}$$

where $\Delta\theta = 2\pi/N$. And thus we arrive at a conclusion that there must be some interface points $\theta_i \in [0, \pi]$ where the following equation holds:

$$\frac{\partial \bar{T}_1}{\partial \bar{r}}(1, \theta_i) < 0 < \frac{\partial \bar{T}_2}{\partial \bar{r}}(1, \theta_i), \tag{44}$$

or some interface points θ_i and $\theta_j \in [0, \pi]$ where the following equations hold:

$$\begin{aligned} 0 < \frac{\partial \bar{T}_1}{\partial \bar{r}}(1, \theta_i) < \frac{\partial \bar{T}_2}{\partial \bar{r}}(1, \theta_i), \\ \frac{\partial \bar{T}_1}{\partial \bar{r}}(1, \theta_j) < \frac{\partial \bar{T}_2}{\partial \bar{r}}(1, \theta_j) < 0. \end{aligned} \tag{45}$$

Physically, this means that near these points θ_i the thermal energy is transferred from the interface to outside (the surrounding fluid) as well as from the interface to inside (the droplet) or near these points θ_i/θ_j the transference of thermal energy from outside/the interface to the interface/outside is weaker/stronger than that from the interface/inside to inside/the interface. On the one hand, if Eq. (44) can satisfy the thermal flux boundary condition in Eqs. (28), thermal sources inside the interface will be introduced to balance the transference of thermal energy. On the other hand, if Eqs. (45) can satisfy the thermal flux boundary condition in Eqs. (28), thermal sinks inside the interface or thermal sources in the droplet will be introduced to decrease the transference of thermal energy from the interface to outside or increase the transference of thermal energy from inside to the interface. Since there are absolutely no thermal sources or sinks inside the interface or thermal sources in the droplet, the above transport processes of thermal energy near the interface seem impossible. It means that the thermal flux across the droplet surface is non-conservative. Moreover, from Eqs. (40, 41), we have

$$\oint \left[k_2 \frac{\partial \bar{T}_2}{\partial \bar{r}}|_1 - \frac{\partial \bar{T}_1}{\partial \bar{r}}|_1 \right] \mathrm{d}s = \frac{\pi}{\epsilon^2} \left(1 + \frac{k_2}{\kappa_2} \right) = \pi \left(1 + \frac{k_2}{\kappa_2} \right) V_\infty Ma. \tag{46}$$

Since both k_2 and κ_2 are positive, we have

$$k_2 \oint \frac{\partial \bar{T}_2}{\partial \bar{r}}|_1 \mathrm{d}s \gg \oint \frac{\partial \bar{T}_1}{\partial \bar{r}}|_1 \mathrm{d}s. \tag{47}$$

From Eqs. (28), we obtain the equivalent integral thermal flux at the boundary

$$\oint \frac{\partial \bar{T}_1}{\partial \bar{r}}|_1 \mathrm{d}s = k_2 \oint \frac{\partial \bar{T}_2}{\partial \bar{r}}|_1 \mathrm{d}s. \tag{48}$$

So, if the thermal flux boundary condition in Eqs. (28) is satisfied, Eq. (47) should be reduced to Eq. (48), which seems impossible. It is termed as a non-conservative integral thermal flux across the surface for the steady thermocapillary droplet migration at large Ma numbers. This implies the overall steady-state energy unbalance of two phases in the flow domain in the co-moving frame of reference.

Equation (47) indicates that at large Ma numbers the integral thermal flux across the surface within the droplet is larger than the surface thermal flux with respect to the continuous phase fluid. However, it should be noted that the droplet migration is, at that time, still in an unsteady state. In the analytical and numerical results [26,27], the steady migration velocity (in direct proportion to Ma) is large at high Ma numbers. Under the condition of large migration velocity, it is unlikely that the order of relevant time scale for the transport process to generate steady velocity and temperature fields is smaller than that for the droplet to move an appreciable distance. So, due to the variation of physical parameters with the ambient temperature, a steady migration process may not be reached. Both experimental results in Fig. 4a, b of [11] and Fig. 4b, d of [28] clearly display that the thermocapillary droplet migration at large Ma numbers is in an accelerating state and does not reach any steady one. Moreover, numerical simulations of the thermocapillary motion of deformable and non-deformable droplets in [18] and the above Sect. 3 indicate that the assumption of quasi-steady state is not valid for large Ma numbers. Thus, it is clear that the invalid assumption of quasi-steady state for the thermocapillary droplet migration process is a reasonable explanation for the non-conservative integral thermal flux across the droplet surface.

5 Conclusion and discussions

In this paper, numerical studies are carried out for thermocapillary migration of a planar non-deformable droplet in two uniform temperature gradients at moderate and large *Ma* numbers by using the front-tracking method. Some calculations at moderate and large *Ma* numbers are performed to analyze the thermocapillary migration for droplets with different sizes. In the range of droplet radius under study, *Re* takes moderate values, and thus the computed flow fields are similar. There appear different types of migration processes in the time frame under investigation depending on the values of *Ma*, which varies within a large range. At moderate *Ma* numbers, after an increase–decrease process in the time evolution of the droplet velocity, the droplet migration reaches a steady state. In the range of large Ma numbers, the oscillation process in the time evolution of the droplet velocity is transformed into a monotonous accelerating process as *Ma* increases. The terminal droplet migration is in an acceleration process and does not reach any steady state. The instantaneous migration velocity at a fixed migration distance decreases with increasing *Ma* number. The numerical simulation results are in qualitative agreement with experimental ones.

Moreover, in comparing the variations of temperature fields inside and outside the droplet, it is evident that at large *Ma* numbers the weak transport of thermal energy from outside of the droplet into inside cannot meet the requirement put forward by the steady migration process, which implies that the advection around the droplet is a more significant mechanism for heat transfer across/around the droplet at large *Ma* numbers.

Furthermore, from the condition of overall steady-state energy balance in the flow domain, we have identified a non-conservative integral thermal flux across the surface for a steady thermocapillary drop migration in a uniform temperature gradient at large *Ma* (*Re*) numbers. It may well result from the invalid assumption of quasi-steady state, and this conclusion implies that the thermocapillary drop migration at large *Ma* (*Re*) cannot reach any steady state and is thus an unsteady process.

We emphasize that all of the above numerical and theoretical results about the thermocapillary migration system of droplets involve assumptions of planar non-deformable interfaces and are subject to constant physical parameters. As mentioned in Sect. 1, the simple modeling is easily applied to explore the dynamical mechanism of droplets, but has potential drawbacks to reproduce the experimental results [28]. The extension to the more realistic case of three-dimensional deformable droplets migrating in a flow field with temperature-dependance physical parameters remains to be implemented.

Acknowledgments We thank Drs. Z. H. Yin, P. Gao and L. Chang for discussions and the IMECH/SCCAS SHENTENG 1800/7000 research computing facilities for assisting in the computation. This work was partially supported by the National Science Foundation through the Grant No. 11172310.

References

1. Leal, L.G.: Laminar Flow and Convective Transport Processes. Butterworth-Heinemann, Boston (1992)
2. Young, N.O., Goldstein, J.S., Block, M.J.: The motion of bubbles in a vertical temperature gradient. J. Fluid Mech. **6**, 350 (1959)
3. Subramanian, R.S.: Slow migration of a gas bubble in a thermal gradient. AIChE J. **27**, 646 (1981)
4. Crespo, A., Jimenez-Fernandez, J.: In: Rath, H.J. (ed.) Microgravity Fluid Mechanics, p. 405, Springer, Berlin (1992)
5. Balasubramaniam, R., Subramanian, R.S.: Thermocapillary bubble migration- thermal boundary layers for large Marangoni numbers. Int. J. Multiph. Flow **22**, 593 (1996)
6. Crespo, A., Migoya, E., Manuel, F.: Thermocapillary migration of bubbles at large Reynolds numbers. Int. J. Multiph. Flow **24**, 685 (1998)
7. Szymczyk, J., Siekmann, J.: Numerical calculation of the thermocapillary motion of a bubble under microgravity. Chem. Eng. Common. **69**, 129 (1988)
8. Balasubramaniam, R., Lavery, J.E.: Numerical simulation of thermocapillary bubble migration under microgravity for large Reynolds and Marangoni numbers. Numer. Heat Transf. A **16**, 175 (1989)
9. Ehmann, M., Wozniak, G., Siekmann, J.: Numerical analysis of the thermocapillary migration of a fluid particle under zero-gravity. ZAMM Z. Angew. Math. Mech. **72**, 347 (1992)
10. Treuner, M., Galindo, V., Gerbeth, G., Langbein, D., Rath, H.J.: Thermocapillary bubble migration at high Reynolds and Marangoni numbers under low gravity. J. Colloid Interface Sci. **179**, 114 (1996)
11. Hadland, P.H., Balasubramaniam, R., Wozniak, G.: Thermocapillary migration of bubbles and drops at moderate to large Marangoni number and moderate Reynolds number in reduced gravity. Exp. Fluid **26**, 240 (1999)
12. Unverdi, S.O., Tryggvason, G.: A front-tracking method for viscous, incompressible, multi-fluid flows. J. Comput. Phys. **100**, 25 (1992)
13. Tryggvason, G. et al.: A front-tracking method for the computations of multiphase flow. J. Comput. Phys. **169**, 708 (2001)
14. Sussman, M., Smereka, P., Osher, S.: A level set approach for computing solutions to incompressible two-phase flows. J. Comput. Phys. **114**, 146 (1994)

15. Nas, S., Tryggvason, G.: Thermocapillary interaction of two bubbles or drops. Int. J. Multiph. Flow **29**, 1117 (2003)
16. Nas, S., Muradoglu, M., Tryggvason, G.: Pattern formation of drops in thermocapillary migration. Int. J. Heat Transf. **49**, 2265 (2006)
17. Haj-Hariri, H., Shi, Q., Borhan, A.: Thermocapillary motion of deformable drops at finite Renoylds and Marangoni numbers. Phys. Fluids **9**, 845 (1997)
18. Herrmann, M., Lopez, J.M., Brady, P., Raessi, M.: Thermocapillary motion of deformable drops and bubbles. Proceedings of the Summer Program 2008, Center for Turbulence Research, 155 (2008)
19. Wang, J., Lu, P., Wang, Z., Yang, C., Mao, Z.-S.: Numerical simulation of unsteady mass transfer by the level set method. Chem. Eng. Sci. **63**, 314 (2008)
20. Wegener, M., Eppinger, T., Bäumler, K., Kraume, M., Paschedag, A.R., B̈ansch, E.: Transient rise velocity and mass transfer of a single drop with interfacial instability-Numerical investigations. Chem. Eng. Sci **64**, 4835 (2009)
21. Zhang, J., Eckmann, D.M., Ayyaswamy, P.S.: A front-tracking method for a deformable intravascular bubble in a tube with soluble surfactant transport. J. Comput. Phys. **214**, 366 (2006)
22. Muradoglu, M., Tryggvason, G.: A front-tracking method for computation of interfacial flows with soluble surfactants. J. Comput. Phys. **227**, 2238 (2008)
23. Braun, B., Ikier, C., Klein, H.: Thermocapillary migration of droplets in a binary mixture with miscibility gap during liquid/liquid phase separation under reduced gravity. J. Colloid Interface Sci. **159**, 515 (1993)
24. Balasubramaniam, R., Chai, A.-T.: Thermocapillary migration of droplets: an exact solution for small Marangoni numbers. J. Colloid Interface Sci. **119**, 531 (1987)
25. Wang, Y., Lu, X., Zhang, L., Tang, Z., Hu, W.: Numerical simulation of drop Marangoni migration under microgravity. Acta Astronautica **54**, 325 (2004)
26. Balasubramaniam, R., Subramanian, R.S.: The migration of a drop in a uniform temperature gradient at large Marangoni numbers. Phys. Fluids **12**, 733 (2000)
27. Ma, X., Balasubramiam, R., Subramanian, R.S.: Numerical simulation of thermocapillary drop motion with internal circulation. Numer. Heat Transf. A **35**, 291 (1999)
28. Xie, J.C., Lin, H., Zhang, P., Liu, F., Hu, W.R.: Experimental investigation on thermocapillary drop migration at large Marangoni number in reduced gravity. J. Colloid Interface Sci. **285**, 737 (2005)
29. Gao, P., Yin, Z., Hu, W.: Thermocapillary motion of droplets at large Marangoni numbers. Adv. Space Res. **41**, 2101 (2008)
30. Gao, P., Yin, Z.H., Hu, W.R.: Numerical investigation of thermocapillary migration of the drop for large Marangoni numbers. Sci. China E **50**, 694 (2007)
31. Bassano, E.: Numerical simulation of thermo-solutal-capillary migration of a dissolving drop in a cavity. Int. J. Numer. Mech. Fluids **41**, 765 (2003)
32. Zhang, J., Miksis, M.J., Bankoff, S.G.: Nonlinear dynamics of a two-dimensional viscous drop under shear flow. Phys. Fluids **18**, 072106 (2006)
33. Delale, C.F., Tryggvason, G., Nas, S.: Cylindrical bubble dynamics: Exact and direct numerical simulation results. Phys. Fluids **20**, 040903 (2008)
34. Peskin, C.S.: Numerical analysis of blood flow in the heart. J. Comput. Phys. **25**, 220 (1977)
35. Someya, S., Munakata, T.: Measurement of the interface tension of immiscible liquids interface. J. Cryst. Growth **275**, c343 (2005)
36. Milne-Thomson, L.M.: Theoretical Hydrodynamics. The Macmillan Press, London (1979)